JOURNAL OF GEOPHYSICAL RESEARCH, VOL. 106, NO. B10, PAGES 21,917–21,934, OCTOBER 10, 2001

Upper mantle anisotropy from long-period P polarization

Vera Schulte-Pelkum, Guy Masters, and Peter M. Shearer

Institute of Geophysics and Planetary Physics, Scripps Institution of Oceanography
University of California, San Diego, La Jolla, California, USA

Abstract. We introduce a method to infer upper mantle azimuthal anisotropy from the polarization, i.e., the direction of particle motion, of teleseismic long-period P onsets. The horizontal polarization of the initial P particle motion can deviate by $>10°$ from the great circle azimuth from station to source despite a high degree of linearity of motion. Recent global isotropic three-dimensional mantle models predict effects that are an order of magnitude smaller than our observations. Stations within regional distances of each other show consistent azimuthal deviation patterns, while the deviations seem to be independent of source depth and near-source structure. We demonstrate that despite this receiver-side spatial coherence, our polarization data cannot be fit by a large-scale joint inversion for whole mantle structure. However, they can be reproduced by azimuthal anisotropy in the upper mantle and crust. Modeling with an anisotropic reflectivity code provides bounds on the magnitude and depth range of the anisotropy manifested in our data. Our method senses anisotropy within one wavelength (250 km) under the receiver. We compare our inferred fast directions of anisotropy to those obtained from P_n travel times and SKS splitting. The results of the comparison are consistent with azimuthal anisotropy situated in the uppermost mantle, with SKS results deviating from P_n and P_{pol} in some regions with probable additional deeper anisotropy. Generally, our fast directions are consistent with anisotropic alignment due to lithospheric deformation in tectonically active regions and to absolute plate motion in shield areas. Our data provide valuable additional constraints in regions where discrepancies between results from different methods exist since the effect we observe is local rather than cumulative as in the case of travel time anisotropy and shear wave splitting. Additionally, our measurements allow us to identify stations with incorrectly oriented horizontal components.

1. Introduction

Classical body wave seismology relies heavily on the travel times of seismic phases. With the advent of global networks of three-component broadband stations, other techniques such as receiver function analysis and S wave splitting measurements have become possible. One relatively unexploited observable is the polarization of P waves.

The term polarization is used for various physical quantities in the literature and requires some clarification. In this paper, we are interested in the direction of particle motion. In the case of P waves, this direction is not identical to that of the wave vector (the normal to the wave front) nor to the ray direction if anisotropy is present [*Crampin et al.*, 1982], and it differs from the angle of incidence at a free surface even for the isotropic case [*Aki and Richards*, 1980; *Bokelmann*, 1995].

Previous particle motion studies [*Park et al.*, 1987b; *Lilly and Park*, 1995; *Jurkevics*, 1988; *Wagner*, 1997; *Vidale*, 1986] concentrated on phase characterization or identification and seismic coda description. *Hu et al.* [1994] used teleseismic P wave polarization in a regional inversion for velocity structure in southern California. (Note that what their study refers to as polarization is the wave vector rather than the particle motion direction.) Mislocation vector studies [*Krüger and Weber*, 1992] and relative array analysis [*Powell and Mitchell*, 1994] also measure the wave vector direction.

Liu and Tromp [1996] and *Hu et al.* [1994] have derived first-order perturbation expressions for polarization (in this instance, ray direction) that can be used in an inversion scheme. These expressions can be compared to the kernels commonly used in travel time tomography inversions based on Fermat's principle. Travel time perturbations are sensitive to velocity variations, while ray directions respond to variations in the

Paper number 2001JB000346.
0148-0227/01/2001JB000346$09.00

gradient of velocity. Therefore, in principle, the two observables could be employed in a complementary fashion in a joint inversion, one defining slow and fast areas and the other delineating their boundaries. The linearized ray direction kernels also show a stronger dependence on the structure on the receiver end of the ray path, whereas the travel time kernels are symmetric with respect to source and receiver. In practice, this means that global travel times mostly reflect the structure of the deep mantle which contains the largest part of the ray path, whereas ray directions are weighted toward near-receiver structure. As a caveat, it should be noted that the wave vector direction in an anisotropic medium will differ from the particle motion and the ray direction, both of which respond to the local anisotropy structure. While particle motion can easily be determined from three-component records and wave vectors can be measured using array data, a ray direction measurement is more difficult to perform.

One advantage of polarization data versus travel times is the independence of polarization with respect to source timing and its insensitivity to source mislocation. These effects lead to significant scatter in absolute travel times, whereas they are negligible in polarization measurements (as pointed out by *Hu et al.* [1994], a typical source location error of 50 km leads to a ray direction error of the order of 0.1%, while the corresponding travel time error is ~5%). Similarly, a typical source time error of 2 s is small enough relative to the length of the time window used for a long-period particle motion measurement that it has no discernible effect.

In the following, we will demonstrate that P wave polarization (in this study, specifically, the azimuth of the initial P particle motion) can be measured reliably from long-period three-component records. The observations show consistency on a regional scale. We will then discuss the possible causative mechanisms and regions for horizontal particle motion anomalies and proceed to eliminate as dominant candidates near-source structure and whole-mantle isotropic heterogeneity, the latter by demonstrating insufficient variance reduction in joint inversions for global mantle structure. The most likely cause for off-azimuth P particle motion is upper mantle anisotropy. In section 5, we fit a simple anisotropic model to our observations and compare the resulting anisotropic parameters to those obtained with other methods. The comparison and additional modeling using a reflectivity code allow us to draw conclusions about anisotropic structure.

2. Method

We used a multitaper frequency domain technique [*Park et al.*, 1987a] to measure the direction of particle motion within one cycle of the P onset (Figure 1).

The method employs orthogonal tapers in the time domain before forming the matrix of eigenspectra of the three components in the frequency domain. A singular value decomposition of the eigenspectra matrix produces, in the presence of a well-polarized signal, one large singular value which is associated with a complex vector defining the direction and phase of particle motion. Multitaper spectral analysis has been applied to complex surface wave and regional body wave signals [*Laske et al.*, 1994; *Park et al.*, 1987a]. In our study, the measurements were performed on P onsets with a high signal-to-noise ratio, which are very simple and linearly polarized, so that some of the characteristics of multitaper analysis (stability with respect to incoherent noise and minimization of spectral leakage) are unneccessary; still, it provides an advantage over simpler techniques [*Vidale*, 1986; *Jurkevics*, 1988] in that it gives a measure of the uncertainty associated with each measurement [*Park et al.*, 1987a].

3. Data

Our data set consists of long-period P arrivals of roughly 6000 teleseismic events recorded at 267 stations of the Global Seismic Network (GSN), including the networks IRIS/IDA, IRIS/USGS, Mednet, Geoscope, Geofon, Terrascope/Trinet, and the U.S. National Network, for the years 1976-1999. Initially, we hand-selected high signal-to-noise ratio events and limited our analysis to source depths of over 100 km in order to avoid contamination by noise and by depth phases. In a second pass through the database we performed an automated calculation of the P arrival signal-to-noise ratio in the long-period (15-100 s) band and analyzed all arrivals with a ratio >5; we also added shallow events to the analysis. Since the results from the second pass were not biased with respect to those from the initial hand-selected small set of deep events,

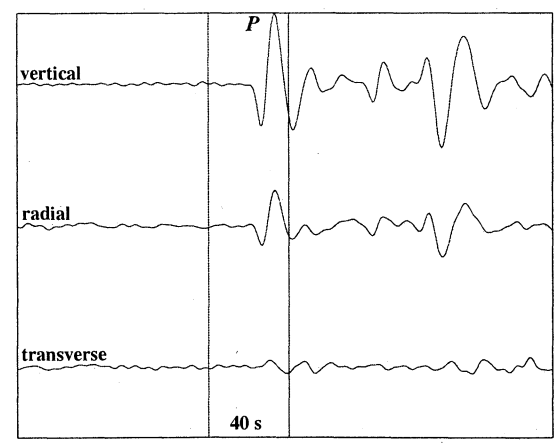

Figure 1. Measurement window for P particle motion. We filter teleseismic P arrivals to around 20 s, rotate onto the station to source azimuth, and analyze the particle motion in a 40 s window around the onset. Note the anomalous energy on the transverse component in this example (PFO record of $m_b = 6.5$ Bolivia event on Julian day 37, 1988).

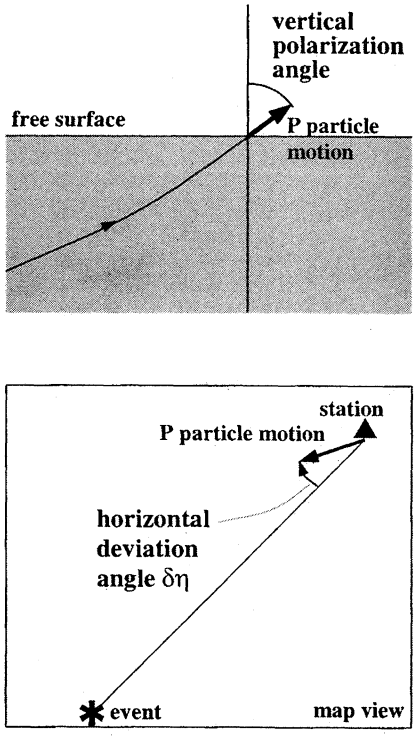

Figure 2. Cartoon of the measured angles of particle motion. (top) Vertical angle and (bottom) horizontal particle motion deviation from the station to event azimuth.

we proceeded with the automated analysis of all source depths, which vastly improved azimuthal coverage at most stations. The data were band-passed in a period range of 15-33 s before measuring the particle motion direction. This period range was chosen to stay within the long-period noise notch.

We determined two angles of the particle motion: the inclination from the vertical in the source-receiver plane, and the rotation of the azimuth of particle motion with respect to the source-receiver great circle (Figure 2). The angle of P wave particle motion in the vertical-radial plane at a free surface is not equal to the incidence angle (defined as the inclination of the incident ray relative to the vertical) owing to conversion of the incoming P wave to SV at the surface. The vertical angle of particle motion ϵ at the free surface is related to the incidence angle as follows [*Aki and Richards*, 1980; *Bokelmann*, 1995]:

$$\epsilon = \arctan \frac{2 \sin i \sqrt{(v_p/v_s)^2 - \sin^2 i}}{(v_p/v_s)^2 - 2 \sin^2 i}, \qquad (1)$$

where v_p and v_s are the P and S velocities of the medium beneath the free surface and i is the subsurface incidence angle. For a realistic range of Poisson ratios the vertical particle motion angle can vary by $\sim 10°$ for the same incidence angle.

The fact that the local surface velocity strongly determines the vertical particle motion angle is visible in Figure 3. The angle of the vertical-radial particle motion is significantly shallower at island stations than at continental stations, which may indicate a higher apparent P velocity. This is consistent with the long-period P wave sensing faster mantle velocities through the thinner oceanic crust. In addition, the picture is complicated by near-surface $P - SV$ conversions. These are used in receiver function analysis at frequencies ~ 1 Hz. In the long-period band of interest in this study, the converted phases interfere within the first cycle of the waveform and distort particle motion. An attempt to invert vertical angles for mantle structure resulted in much lower variance reduction than an inversion of the horizontal particle motion. We will therefore concentrate on the more consistent horizontal angles for the remainder of the paper.

Although the particle motion of the P onset is usually highly linear, its azimuth is in most cases not aligned with the great circle between source and station, as would be expected for a P wave in a spherically symmetric, isotropic Earth model. This means that there is a slight transverse motion of the P onset, a phenomenon which could be attributed to P bending by heterogeneous structure, P to SH conversion by inclined boundaries, or anisotropy within a depth range of the order of one wavelength (in our case, 60-270 km) beneath the receiver. Apparent transverse P particle motion can also be an artifact caused by misorientation or miscalibration of a sensor's horizontal components.

The transverse motion corresponds to a clockwise or counterclockwise rotation of the azimuth of P motion relative to the great circle azimuth (Figure 2). We plot the rotation of each P arrival as a function of back azimuth and vertical angle of incidence at the station as shown in Figure 4.

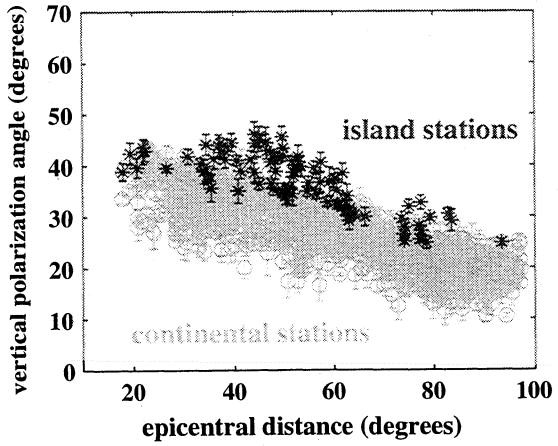

Figure 3. Vertical particle motion angle as a function of epicentral distance. Measurements from island stations are solid symbols, all others are shaded. The errors are determined individually by the multitaper analysis. There are a total of 1328 measurements of deep events, 97 of which are from island stations.

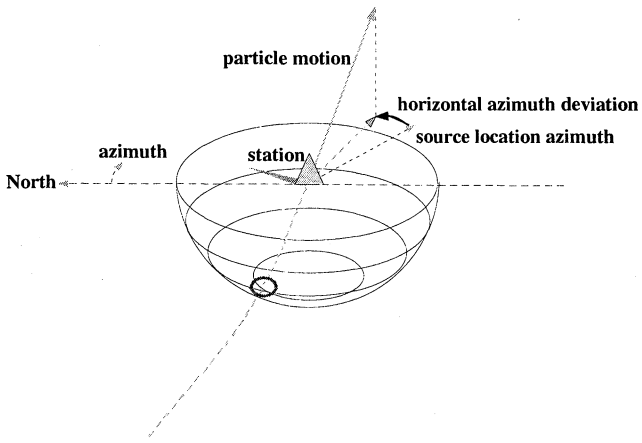

Figure 4. Explanation of the plots of azimuthal deviation patterns in Figure 7 and Figure 9. For a specific station we project the measurements onto the hemisphere underneath. A clockwise deviation of the horizontal particle motion from the station to source azimuth is plotted as a cross, scaled by the size of the deviation. On the hemisphere, the cross is plotted at the back azimuth of the source location and at the incidence angle of the PREM ray. Counterclockwise deviations are plotted as circles.

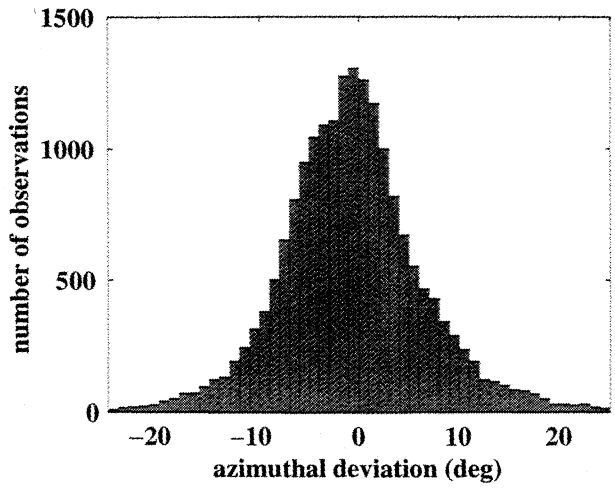

Figure 6. Histogram of the global data set of azimuthal particle motion deviation. The median is -0.9°, the scaled median absolute deviation (SMAD) is 7.2°. The nonzero mean and skewness reflect the fact that a significant number of stations are misoriented (see Appendix A) and that azimuthal coverage is limited at many stations.

4. Observations

We selected measurements with a highest singular value of over 0.82 of the eigenspectra matrix, which indicates that a single well-polarized signal is present. In these cases, the motion is usually highly linear (Figure 5). Despite the uncomplicated character of motion, we frequently observe horizontal deviations from the great circle azimuth in excess of 10°. The average measurement error given by the multitaper analysis is 3.8°.

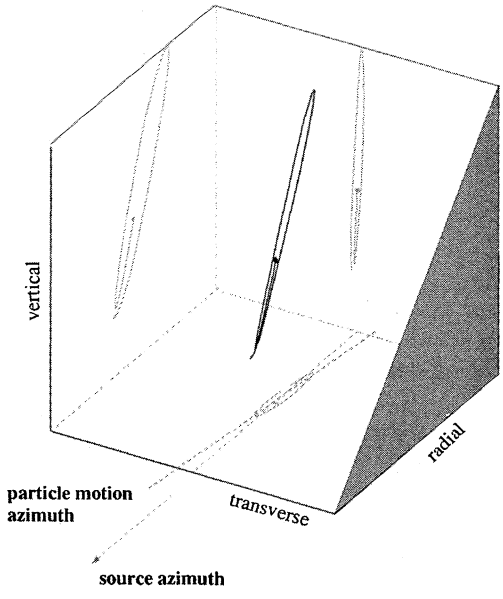

Figure 5. Hodogram (solid, with shaded projections) for the rotated *P* onset shown in Figure 1. The particle motion is very close to linear, yet there is a significant transverse component.

At 264 out of 267 stations we were able to obtain measurements that fulfilled our singular value quality criterion, with a median number of 60 observations per station. Figure 6 shows a histogram of the entire data set. We show later that the measured deviations are an order of magnitude larger than those predicted by both spherical harmonic three-dimensional (3-D) mantle models such as S16b30 [*Masters et al.*, 1996] and SKS12_WM13 [*Dziewonski et al.*, 1996] and high-resolution mantle models from block tomographic inversions [*Grand et al.*, 1997; *Grand*, 1994; *Masters et al.*, 2000].

When plotted on station hemispheres as described in Figure 4, the azimuthal deviations exhibit clear large-scale patterns. A few examples are shown in Figure 7. This is unlikely to be an effect of the immediate subsurface. The same analysis performed in the short-period band (near 1 Hz) yields patterns that are as clear yet show no resemblance to the long-period case. We show later that there is a high consistency of the patterns over distances of several 100 km, which also breaks down at short periods. We can also exclude the close vicinity of the source as the generating area since the patterns remain consistent between shallow and deep events. Therefore our signal is most likely to stem from the mantle. We will attempt to interpret this result by forward modeling and inversion in section 5.

5. Interpretation

5.1. Global Isotropic Mantle Heterogeneity

Our first approach was to explain the azimuthal anomalies in the framework of a global inversion for isotropic 3-D mantle structure, similar to body wave travel

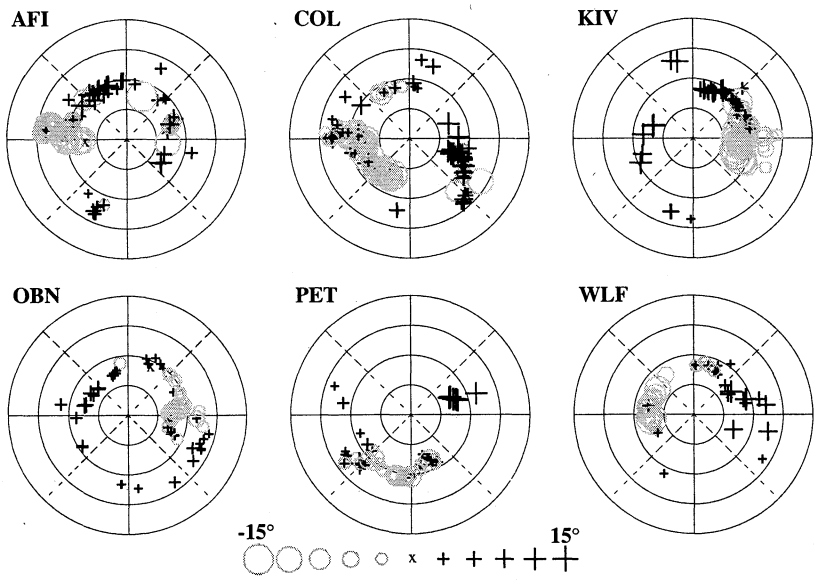

Figure 7. Examples for azimuthal deviation patterns of horizontal *P* particle motion as described in Figure 4 at stations AFI (Samoa), COL (Alaska), KIV (Russia), OBN (Russia), PET (Kamchatka), and WLF (Luxembourg). The concentric circles show 10° increments of incidence angle of the PREM ray; north is up.

time residuals. *Dziewonski* [1984] and many subsequent travel time tomography studies have used the following linearized inversion approach. If one assumes that the unknown velocity structure (such as lateral velocity variations) is a small perturbation to a known background structure (e.g., a spherically symmetric Earth model), the travel time integral over the true ray path can be replaced by a first-order approximation, where the velocity perturbations are integrated over the unperturbed ray path in the background model [*Liu and Tromp*, 1996]:

$$\delta T = -\int_0^{\Delta} \frac{r}{\sin i}\frac{\delta v}{v^2} d\phi \,, \tag{2}$$

where v is the spherical background velocity model, δv is the velocity perturbation, and the integration is performed along the radial and azimuthal coordinates (r, ϕ) along the ray path in the unperturbed medium to distance Δ. The first-order assumption is that the ray path is not perturbed significantly.

An equivalent first-order expression can be derived for the ray directions. The off-azimuth horizontal perturbation in ray direction takes the following form [*Liu and Tromp*, 1996]:

$$\delta\eta = \frac{1}{\sin\Delta}\int_0^{\Delta} \frac{\sin\phi}{\sin^2 i}\frac{1}{v}\frac{\partial\delta v}{\partial\theta} d\phi \,, \tag{3}$$

where θ is the cross-ray angular coordinate. Note that travel times see the velocity perturbation δv, whereas the horizontal arrival angle is sensitive to the cross-ray velocity perturbation gradient $\partial\delta v/\partial\theta$. This indicates that arrival angle anomalies can be used to delineate the boundaries of velocity anomalies and are more sensitive to small-scale structure than travel times. Also, the travel time kernel is symmetric about the turning point of the ray, whereas the $\sin\phi$ term in the horizontal angle kernel weights the sensitivity toward the receiver.

We found that this linearized expression provides excellent agreement with results from nonlinear ray tracing for current global 3-D mantle models, as did *Liu and Tromp* [1996] for SKS12_WM13 [*Dziewonski et al.*, 1996]. However, both ray tracing and first-order perturbation theory predict angles that are an order of magnitude smaller than those we observe in our data. This holds not only for low-degree spherical harmonic models like SKS12_WM13 and S16b30 [*Masters et al.*, 1996] but also for models derived from block inversion which contain higher wave number structure. We performed forward modeling using a degree 40 expansion (corresponding to 5° resolution) of high-resolution 3-D mantle models [*Grand*, 1994; *Grand et al.*, 1997; *Masters et al.*, 2000]. Both mantle models produce maximum anomalies of 2° and a scaled median absolute deviation (SMAD) of the anomalies of 0.5°. Compare this to our observed values in Figure 6 of anomalies exceeding 15° and an SMAD of 7.2°. The character of the predicted polarization residuals at the stations is also very different from our observations (Figure 7), exhibiting much faster variation with back azimuth than we see in the data, in addition to the magnitude discrepancy.

Even high-resolution global tomographic mantle models show a falloff in their amplitude spectra toward higher wave numbers. It may therefore come as no surprise that they do not contain lateral gradients high enough to reproduce our observations since the lateral gradient amplitude spectrum is merely the velocity amplitude spectrum scaled by wave number. To

test whether inclusion of polarization data would result in larger amplitude small-scale structures, we performed a global inversion of our data jointly with long-period teleseismic P and PP-P travel times, surface wave phase velocities, and free oscillation mode coefficients [*Masters et al.*, 1996, 2000] with lateral resolution up to degree 24. Increasing the lateral resolution did not improve the fit, and the variance reduction of the polarization data in the joint inversion was no more than 16%. In conclusion, our modeling and inversion experiments suggest that the lower mantle is not a likely candidate as a cause of long-period P polarization anomalies.

5.2. Regional Heterogeneity and Anisotropy

Having excluded the near-source area (based on the lack of dependence on source depth and mechanism) and the lower mantle as the regions which give rise to azimuth anomalies, we now focus on the upper mantle and crust near the receivers. A comparison between residual patterns for different stations shows strong consistency of the patterns over distances of several hundred kilometers. We demonstrate this fact later in this section with examples from California, where our station density is highest. This and the independence of the residuals with respect to source depth indicate that the cause of the azimuthal deviations lies on the receiver side rather than the source side of the ray path. The consistency on a regional scale suggests a location either in the upper mantle or a uniform pattern at shallower depths, e.g., anisotropy. A very shallow source is unlikely since the regional consistency breaks down for the same analysis performed in the short-period band.

Our off-azimuth particle motion signal is essentially a P arrival that has a transverse component. There are several ways to create such motion. One is bending or refraction out of the radial-vertical plane by lateral heterogeneities, e.g., nonhorizontal velocity gradients or inclined interfaces. Dipping interfaces also cause P to SH conversions which will additionally affect the long-period particle motion of the P onset if they occur close to the surface. Simple modeling using Snell's law shows that a Moho dip of 10° beneath a station causes azimuthal deviations of the amplitude we observe in the data. A dipping interface results in a $\sin\eta$ pattern (η is azimuth of incidence) as in Figure 8 (left). Interface curvature leads to $\sin(2\eta)$ components in the azimuthal pattern.

An alternative cause for P particle motion outside the radial/vertical plane is the presence of anisotropy within a few wavelengths of the receiver [*Levin and Park*, 1998; *Bostock*, 1998]. For our period range of 15-33 s, one wavelength translates to ~60-270 km depth. In an anisotropic medium the first arrival would be the quasi-P (qP) phase. The particle motion of qP is not aligned with the direction of propagation (ray direction) nor with the normal on the wave fronts, in contrast to isotropic P [*Crampin et al.*, 1982].

The simplest model, transverse isotropy (i.e., hexagonal anisotropy with a vertical symmetry axis), fails to explain our observations since it causes no azimuthal deviations or $P-SH$ coupling. The same hexagonal anisotropy with a horizontal axis of symmetry, however, leads to a characteristic, predominantly $\sin(2\eta)$ periodic pattern of azimuthal deviation (Figure 8, middle). This geometry could result from both olivine crystal alignment in the mantle [*Christensen*, 1984] and microcracks in the crust [*Shearer and Chapman*, 1989]. These are likely candidates for the cause of crustal and mantle anisotropy.

Azimuthal $\sin\eta$ signatures have in the past been attributed to a dipping Moho [*Lin and Roecker*, 1996], and $\sin(2\eta)$ patterns to anisotropy [*Vinnik and Montagner*, 1996; *Girardin and Farra*, 1998]. However, a

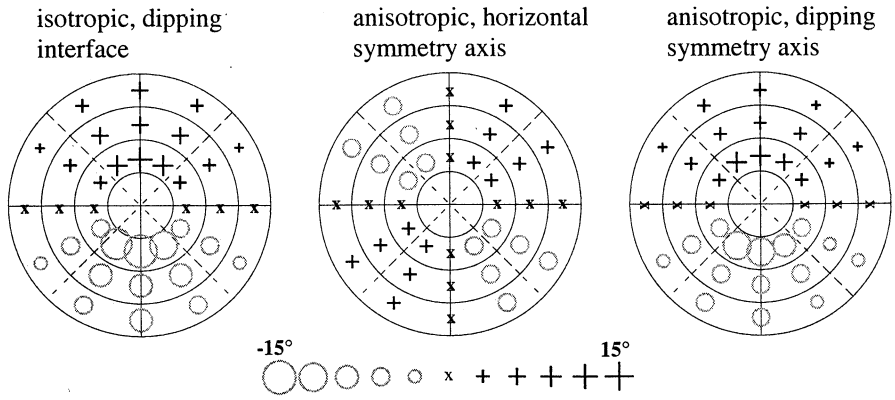

Figure 8. Azimuthal particle motion anomaly patterns as described in Figure 4. (left) Pattern for a Moho dip of 10° to the west, no anisotropy. (middle) Pattern for a horizontally stratified model with 8% anisotropy in a 30 km thick layer at the top. The anisotropy is hexagonal with a horizontal symmetry axis oriented E-W. (right) Same as middle, except the symmetry axis is tilted 45° down towards east. Concentric circles show 10° increments of incidence angle. North is up.

distinction between dipping interfaces and anisotropy based on this periodicity difference alone can be misleading. In the isotropic case, interface curvature can still lead to a $\sin(2\eta)$ pattern. In the case of anisotropy, a tilt away from the horizontal of the symmetry axis for the hexagonal case breaks down the $\sin(2\eta)$ symmetry and can produce a pattern identical to that caused by a dipping interface (Figure 8, right). It is therefore impossible to distinguish between heterogeneity and anisotropy for a single station from particle motion alone. The same observation has been made for transverse component receiver functions [*Savage*, 1998].

In our case, we can still make inferences about heterogeneity versus anisotropy by comparing azimuthal patterns at several stations in the same region. The best suited region with our current data set is California, where the station density is highest and we also see very pronounced patterns of azimuthal particle motion deviations.

Travel time tomography studies have found strong velocity anomalies, e.g., the Isabella high-velocity body and the Transverse Range anomaly [*Humphreys and Clayton*, 1990]. The Moho also shows significant topography through the region [*Richards-Dinger and Shearer*, 1997; *Zhu and Kanamori*, 2000; *Baker et al.*, 1996]. Anisotropy has also been found by *Polet* [1998], *Hearn* [1996], *Smith and Ekström* [1999], and *Savage and Sheehan* [2000].

The azimuthal particle motion deviation patterns are consistent through a large part of southern California, as Figure 9 shows. The scale of consistency makes it unlikely that conversions or out-of-plane refraction at the Moho cause the observed patterns in P since postulated Moho topography [*Zhu and Kanamori*, 2000; *Richards-Dinger and Shearer*, 1997] varies widely between stations with very similar patterns. The same argument also holds for relatively small-scale velocity anomalies such as the Isabella and the Transverse Range high-velocity bodies. Their presence and orientation relative to the stations does not seem to affect the pattern since it is also seen at other stations without similar strong velocity variations in their vicinity.

In order to investigate whether deep upper mantle heterogeneity could cause the common pattern, we plotted the IASPEI ray paths for the observed events at each station (Figure 10). The lack of overlap between ray paths to 410 km depth shows that the station spacing is large enough and the ray incidence angles are sufficiently steep to prohibit a single mantle feature above the transition zone from causing identical patterns at all stations which exhibit consistency. This holds even when taking into account the Fresnel zones around the rays (for instance, the $\lambda/4$ Fresnel zone at 150 km depth for the longest period of 33 s is 2° wide).

Although this still leaves open the possibility that the correlation in pattern between stations could result from more distant (i.e., deep-mantle) heterogeneity, such heterogeneity would need to be much larger than current spherical harmonic models of the whole mantle suggest, as we concluded in section 5.1. In addition, we show in section 5.3 that rapid changes in patterns occur going from one region of consistency to another, which again speaks against a source-side or deep-mantle origin. We also demonstrate in the following that the assumption of upper mantle anisotropy leads to reasonable agreement with results from anisotropy studies using different seismic phases.

We conclude that uniform anisotropy in the upper mantle is the most likely cause for the consistent particle motion patterns in this region. The depth range for anisotropy can be inferred from comparison with anisotropy measurements using other phases and through a comparison with modeling results in section 5.4.

5.3. Anisotropy Fit

Under the assumption that any $\sin(2\eta)$ component of azimuthal deviation can be ascribed to anisotropy, we performed a fit of fast direction and anomaly amplitude on the global set of stations. The fit of $\sin(2\eta)$ patterns allows us to perform a comparison with anisotropy fast directions and strength derived from other phases and make inferences about the existence and depth extent of anisotropy.

Since we lack constraints on the anisotropy-heterogeneity tradeoff based on dense station coverage except for California, the detection of a $\sin(2\eta)$ component is a necessary condition for the existence of horizontally symmetric anisotropy but will not allow us to exclude heterogeneity such as curvature on interfaces as an alternative source for most stations. Also, failure to detect a $\sin(2\eta)$ pattern still leaves open the possibility of the existence of dipping hexagonal or non-hexagonal anisotropy. Our present data set does not allow us to invert for more complicated models of anisotropy. However, a favorable comparison with results from other methods in section 5.5 suggests that horizontal azimuthal anisotropy is a valid first-order assumption. An additional source of misinterpretation is possible nonorthogonal orientation of horizontal sensor components or incorrect gains in the instrument responses, which may both mimic a $\sin(2\eta)$ anomaly and are also difficult to exclude for stand-alone stations.

A $\sin(2\eta)$ fit is justified by the proof given by *Backus* [1965] that weak anisotropy can be described by a sum of $\sin(2\eta)$ and $\sin(4\eta)$ variations in travel time. The azimuthal periodicity of travel times is that of the slowness surface, while the group velocity direction is the normal on the slowness surface. For general anisotropic symmetries, the qP wave particle motion directions follow group velocity directions closely [*Crampin et al.*, 1982]. Since travel time studies commonly find mostly 2η variations and insignificant 4η terms, we make the same assumptions about weak anisotropy and the predominance of the 2η over 4η terms for particle motion.

For each of the azimuthal deviation patterns, such as shown in Figure 9, we divided the observed values into

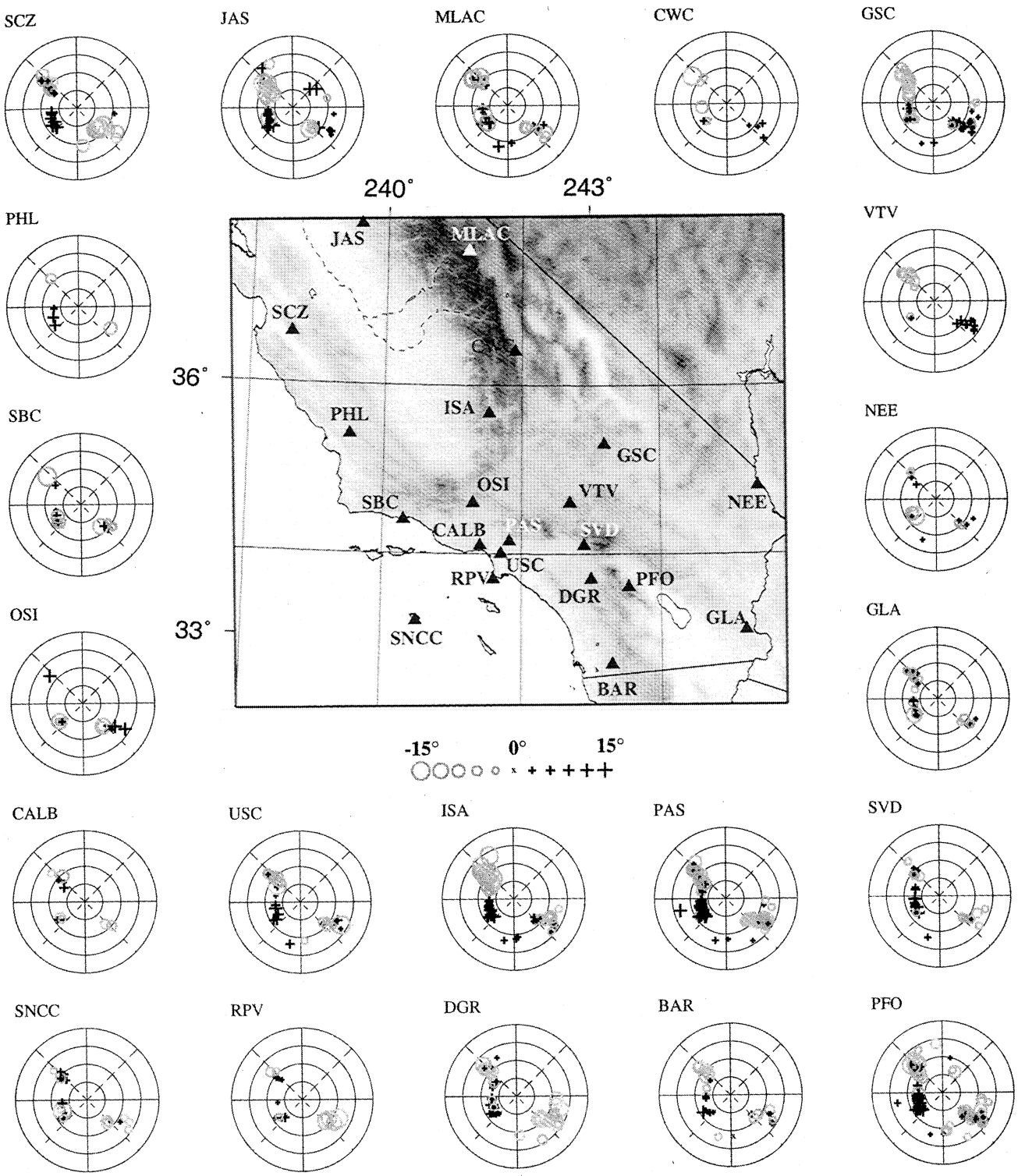

Figure 9. Azimuthal deviation patterns at stations in California, as described in Figure 4. The concentric circles show increments in incidence angle of 10°, north is up.

azimuthal bins of 20° and formed the median in every bin containing more than five individual measurements. The SMAD within the azimuthal bin gives us a measure of the error associated with the median value. If a station has at least six bins with a median calculated in this fashion and the bins are distributed over at least three azimuthal quadrants, we fit the following pattern to the medians:

$$\delta\eta = \eta_0 + a\sin\eta + b\cos\eta + c\sin(2\eta) + d\cos(2\eta), \quad (4)$$

using least squares. The constant term takes into ac-

count station misorientation (see Appendix A), and the $\sin\eta$ and $\cos\eta$ terms may reduce the influence of heterogeneity. The fast direction is then approximated as

$$\eta_{\text{fast}} = \frac{1}{2}\arctan\frac{c}{d} + \pi/2, \quad (5)$$

and the anomaly amplitude ascribed to anisotropy is

$$\delta\eta_{\max} = \sqrt{c^2 + d^2}. \quad (6)$$

The results, with errors propagated through the least squares fit, are shown in Figure 11[1]. There was sufficient azimuthal coverage to obtain an estimate of horizontal anisotropy at 75 of 264 stations. At 50 of these stations, the detected anomaly amplitude exceeded its uncertainty. The anomaly amplitudes, i.e., the maximum amplitude of the $\sin(2\eta)$ pattern, have a range of up to 6.4° of off-azimuth particle motion attributable to horizontal azimuthal anisotropy. The median error is 1.8° at the set of stations with significant signal (i.e., where the 2η amplitude is larger than the associated error).

Fast directions and amplitudes in southern California are consistent within the errors of the fit. Elsewhere, the station spacing is rather large for station-to-station comparisons. There appears to be possible long-range consistency between stations in Southeast Asia, eastern Siberia, the northern part of North America, and Australia.

The measurements are somewhat spotty in a global sense, but nevertheless, some patterns are discernible. Broadly speaking, the observed directions can be divided into two classes. In orogenic belts and at active margins we see fast orientations parallel to arcs and transform faults and perpendicular to convergence. Under continental cratons we find alignment with absolute plate motion directions.

Anisotropy in the upper mantle is currently attributed to alignment of olivine and perhaps other mantle minerals, although influence from oriented inclusions cannot be excluded [*Kendall*, 2000]. The question is then whether the preferred orientation is related to deformation in the lithosphere [*Silver*, 1996] or whether the upper mantle is decoupled from the overlying plate so that the anisotropy reflects asthenospheric flow [*Vinnik et al.*, 1992].

A majority of the fast directions we observe suggests orientation parallel to subduction and collision zones and strike-slip plate boundaries. We see subduction-parallel fast directions in Japan, New Zealand, Guam, and Samoa. Splitting studies have found both trench-parallel and trench-perpendicular fast directions, depending on the subduction zone [*Kendall*, 2000]. P_n studies have also indicated both cases [*Hearn*, 1999]. *Smith and Ekström* [1999] obtain mostly boundary-parallel fast orientations in subduction zones and orogenic belts in a global P_n study. *Russo and Silver* [1994] and *Hearn* [1999] propose mechanisms for orientations both perpendicular and parallel to trenches. Our data set mostly suggests the latter. Regardless of which of the two cases is observed, there is clear evidence for a correlation with surface tectonics in subduction zones. Our results also show other areas with convergent plate motion where the fast direction is perpendicular to the direction of convergence (Alaska, southern Europe, and China), which again supports lithospheric coupling. This has also been observed using SKS (e.g., *Vinnik et al.* [1992]) and P_n [*Smith and Ekström*, 1999]. R. Meissner et al. (Seismic anisotropy and mantle creep in young orogens, submitted to *Geophysical Journal International*, 2001) explain anisotropy parallel to the structural axis of orogens by extension of crustal escape tectonics [*Molnar and Tapponnier*, 1975] into the uppermost mantle.

We also see fast directions parallel to shear zones. Examples are the San Andreas fault in California, the North Anatolian fault in Turkey, transform faults related to the India-Asia collision in Southeast Asia [*Molnar and Tapponnier*, 1975], and eastern Siberia [*Vinnik et al.*, 1992]. This orientation parallel to strike-slip faults again supports a strong influence of lithosperic strain on mantle anisotropy. Similar results are observed for SKS [*Savage*, 1999] and P_n [*Smith and Ekström*, 1999].

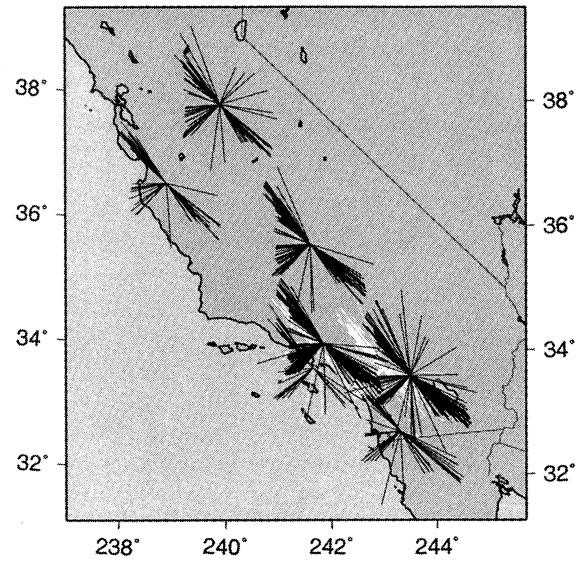

Figure 10. IASPEI ray paths for California stations with consistent azimuthal deviations, shown as black lines (and as white lines for two stations to aid distinction). The path for each measurement at stations BAR, PFO, DGR, RPV, USC, PAS, SVD, ISA, SCZ, and JAS in Figure 9 is shown to a depth of 410 km.

[1]Supporting table is available via Web browser or via Anonymous FTP from ftp://kosmos.agu.org, directory "apend" (Username = "anonymous", Password = "guest"); subdirectories in the ftp site are arranged by paper number. Information on searching and submitting electronic supplements is found at http://www.agu.org/pubs/esupp_about.html.

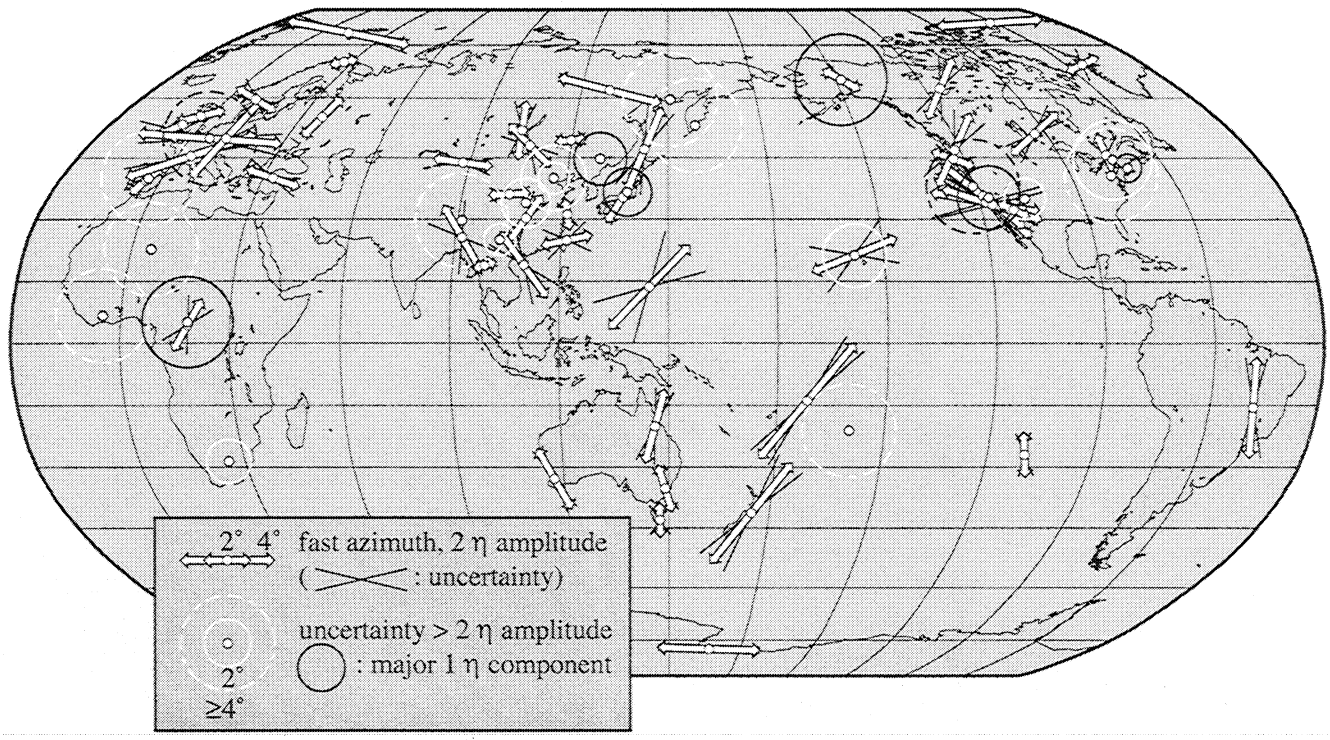

Figure 11. Fast directions and 2η anomaly amplitudes from a least squares fit of $\sin(2\eta)$ patterns to the observed azimuthal P polarization anomalies. The length of the arrows is proportional to the anomaly amplitude. The azimuthal uncertainty of the fast directions is indicated by black lines. White circles indicate an upper bound of the 2η amplitude where the uncertainty of the 2η signal was greater than its amplitude. Amplitude uncertainties larger than 4° are shown as dashed lines. At stations where the inconclusive fit is partly due to a strong 1η azimuthal component (dipping anisotropy or dipping interface), the upper bound on 2η is shown in black. A number of the stations with resolvable signal also have an additional 1η component, but this is not shown for the sake of simplicity.

For stable continental areas, our results appear to suggest some correlation with absolute plate motion directions. The NE-SW fast directions in Canada and N-S in Australia agree with the plate velocity directions in the HS2-NUVEL1 absolute plate motion model by *Gripp and Gordon* [1990]. There may also be agreement in Africa, although we only have a fit at a single station and the HS2-NUVEL1 absolute plate velocity is much smaller than for North America and Australia. The N-S orientation of the single measurement we obtained in Brazil does not agree with the modeled plate motion direction, which is close to E-W.

The comparison with the strike of tectonic features and absolute plate motion allows some inferences about the depth of anisotropy and the mechanism for alignment. Our observations support the influence of lithospheric strain in areas of tectonic activity and orientation due to asthenospheric flow underneath cratons. To address the question whether part of the tectonic signature could be due to crustal deformation and to develop a more detailed framework in general for the degree of anisotropy and the depth ranges involved, we performed numerical modeling as well as a comparison with results from other observational studies on anisotropy.

5.4. Anisotropic Reflectivity Modeling

We used a layer matrix method [*Kennett*, 1983; *Chapman and Shearer*, 1989; *Booth and Crampin*, 1985; *Fryer and Frazer*, 1984] to model finite frequency effects of anisotropic layers in a horizontal layer stack. Since our observations suggest that the effects of interest take place in the top several 100 km beneath the station, we chose plane P waves incident on a Cartesian model. Apart from a slowness integration, which in our case of an incident plane wave is redundant, this method is equivalent to a full reflectivity formulation. We calculated responses of stacks of anisotropic and isotropic layers at a range of frequencies. The responses were transformed into the time domain which results in seismograms consisting of a series of delta functions, to which we then applied the same band filters we used for our data.

In the high-frequency limit the deviation of qP particle motion from the slowness azimuth is a strictly local phenomenon. As soon as the wave front leaves an anisotropic layer, the P motion realigns with the slowness (phase velocity) and propagation (group velocity) azimuths, and the orthogonal qP component continues

to propagate as an S phase. This is an important distinction to the cumulative effect of anisotropy in shear wave splitting: P particle motion is sensitive to anisotropy only within a wavelength of the receiver. In the finite frequency case, an isotropic layer whose thickness is small compared to the wavelength will be transparent to effects of anisotropy underneath. In effect, the incident and converted pulses are broadened and interfere with each other in the band-limited case.

We modeled the depth extent to which anisotropy can still be detected through an overlying isotropic layer using a simple crust and mantle model. For increasing depths of the isotropic to anisotropic transition we determined the magnitude of the particle motion deviation at the surface. The anisotropy model was the same as assumed in the least squares fit to our data, i.e., hexagonal anisotropy with a horizontal symmetry axis, and we set the strength of the anomaly to 10% P velocity anisotropy between the fast and slow axis. This is the maximum value postulated by *Smith and Ekström* [1999] for the uppermost mantle.

A surface signal larger than the median amplitude standard error of 1.8° in our data fit can be observed for depths of the top of the anisotropic layer of 250 km and less. This makes 250 km an upper bound for the thickness of the isotropic range through which our technique could have detected a deeper anisotropic layer. We also tested for the minimum thickness at which an anisotropic layer gives rise to a significant signal. A layer thickness of at least 8 km is required to cause an anomaly amplitude larger than our median uncertainty. This is for the case of 10% anisotropy; weaker anisotropy will increase the minimum detectable thickness.

An increase in the observed anomaly occurs to an anisotropic layer thickness of 60 km. Further increases in the thickness lead to a slight falloff in the anomaly magnitude, which then settles to an asymptotic value near 200 km. The slight decrease with increasing thickness is due to interference with a phase that converts from P to quasi-S at the bottom of the anisotropic layer and continues as an SH arrival with opposite polarity from the top of the layer. The minimum strength of anisotropy to cause an anomaly larger than our median uncertainty is 2% for a layer thickness of 60 km. Thinner layers will require stronger anisotropy to be detected within the constraints given by our method and average azimuthal coverage.

Even the largest anomaly of 6.5° we obtained from our $\sin(2\eta)$ fit can be fit with reasonable anisotropy models. Examples of models that produce such an anomaly with our reflectivity code are 8% anisotropy in a 60 km thick layer in the lowermost crust (bottom 10 km of a 30 km crust) and uppermost mantle, or 6% if a deeper anisotropic layer with a change in fast direction is added. The median amplitude we observed at stations with significant signal is 2.8°. If we restrict the anisotropy to the upper mantle, we can model this value with a 30 km isotropic crust overlying a 6% anisotropic layer of 60 km thickness in the upper mantle. The same value can be obtained with 8% anisotropy in the top 20 km of the mantle. A high anomaly value of 5° that we observed at several stations can be modeled with 10% anisotropy in a 60 km thick uppermost mantle layer. As we see, the forward modeling of the $\sin(2\eta)$ anomaly amplitude with multiple anisotropic layers is highly nonunique. Therefore we have limited our modeling to finding the extreme values of resolvable parameters of anisotropy and suggestions for typical values for a simple model. An exact fit will be left to a subsequent frequency-dependent analysis which will provide additional constraints.

Many SKS splitting studies explain azimuthal variation of splitting parameters as averaging over multiple layers of anisotropy, and the averaging behavior has been studied theoretically [*Saltzer et al.*, 2000; *Rümpker and Silver*, 1998]. In the case of P particle motion, we have the advantage that averaging only occurs over a depth range of a wavelength from the receiver. The averaging, however, is not linear with depth. Our modeling indicates that the observed values are strongly weighted toward shallower layers.

To summarize our modeling results, the stations with significant signal in our least squares fit indicate, on average, the following minimum criteria for anisotropy structure: an anisotropic layer thickness of at least 8 km, anisotropy at depths shallower than 250 km, and at least 2% P velocity contrast between the fast and slow axes. Stations with errors smaller than the median standard deviation will be able to detect a weaker signal. Even our largest polarization anomaly can be fit with 8% anisotropy. Possible sources for misinterpretation are heterogeneity and also relative misorientation or miscalibration of horizontal sensor components, unless we are in a region with a consistent signal at several stations. In the light of these bounds on the observed P particle motion anisotropy, we next perform a comparison with results obtained via other techniques which have different depth and strength sensitivities in the hope to further constrain anisotropic parameters.

5.5. Comparison With P_n and SKS Results

We compare our results with those from a global P_n travel time study by *Smith and Ekström* [1999] and with SKS splitting parameters. The SKS results are from the compilations by *Silver* [1996] and *Savage* [1999], with additions from *Savage et al.* [1996], *Pondrelli and Azzara* [1998], *Wolfe and Solomon* [1998], *Barruol et al.* [1998], *Fabrititus* [1995], and *Wolfe et al.* [1999]. The SKS results not in the *Silver* [1996] and *Savage* [1999] compilations were taken from the SKS splitting reference web page compiled by D. L. Schutt (www.ciw.edu/schutt/anisotropy_resource/aniso_source.html). The comparison is shown in Figure 12, with closeups in Figures 13 and 14.

The first question to address is whether the agreement between the methods is better than random. Fig-

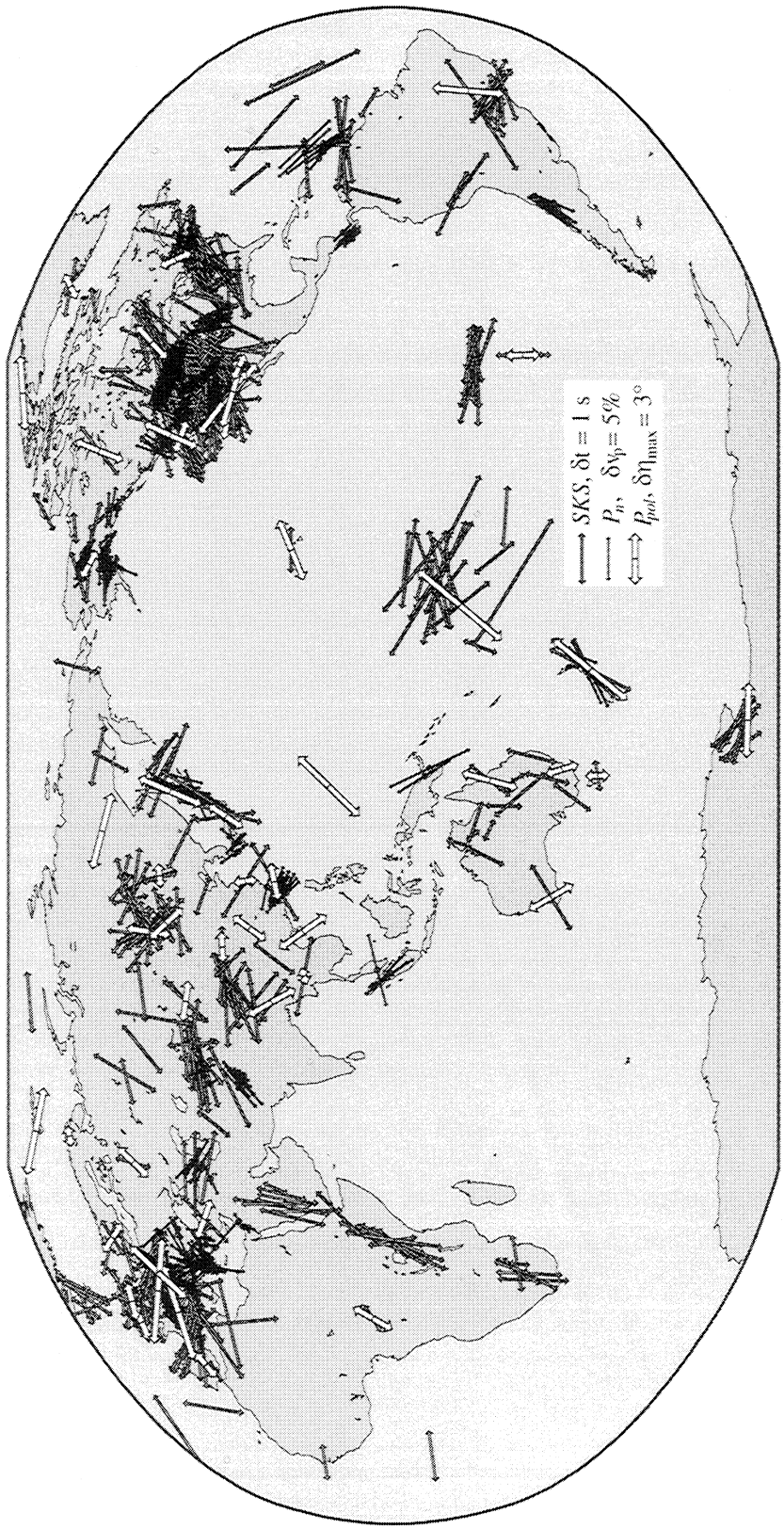

Figure 12. Comparison of anisotropic parameters from P polarization (white arrows), SKS splitting (grey arrows) and P_n travel times (black arrows). Fast directions are indicated with arrow lengths proportional to anomaly amplitudes (percent variation of P_n velocity, SKS splitting time in seconds, and $P_{\mathrm{pol}}\sin(2\eta)$ maximum anomaly in degrees, respectively). In a hexagonally anisotropic medium with a horizontal axis of symmetry, all three directions coincide.

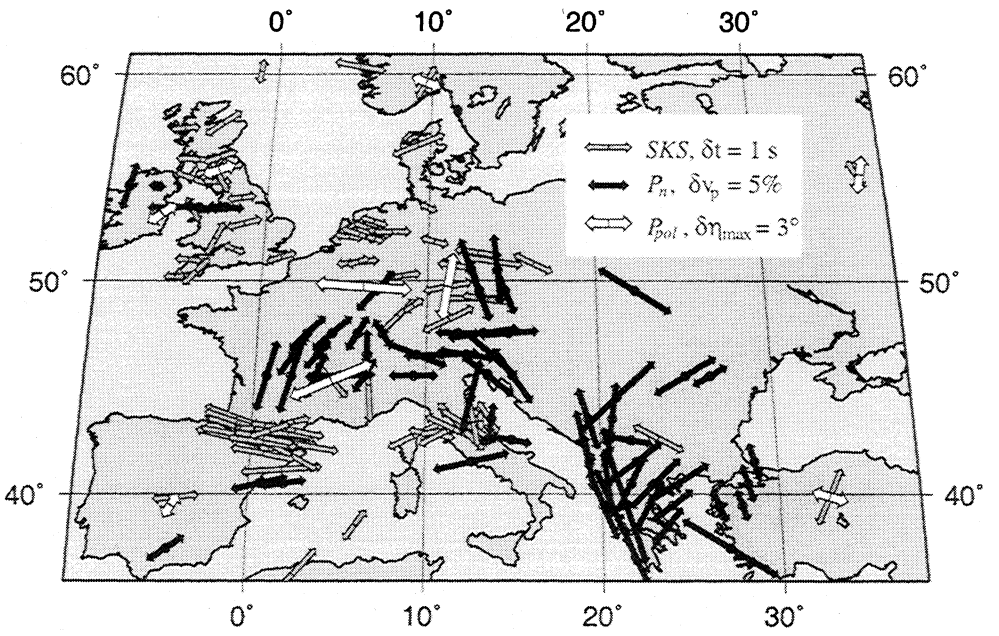

Figure 13. Comparison of anisotropic parameters from P_{pol} (white arrows), SKS (grey arrows) and P_n (black arrows): a closeup of Europe in Figure 12.

ure 12 suggests that it is, but since a map comparison of axial data by eye may be misleading, we also evaluated the distributions of the angular separation of P versus P_n and SKS statistically.

Figure 15 shows a histogram of the difference between P polarization and P_n travel time axial fast directions. To avoid confusion with fast directions inferred from P travel times, we will hereinafter refer to our results from P polarization as P_{pol}. We compare pairs of P_{pol} and P_n samples that lie within 5° caps over the globe (comparisons by station are not possible since the P_n values are obtained by a station pair method). If there

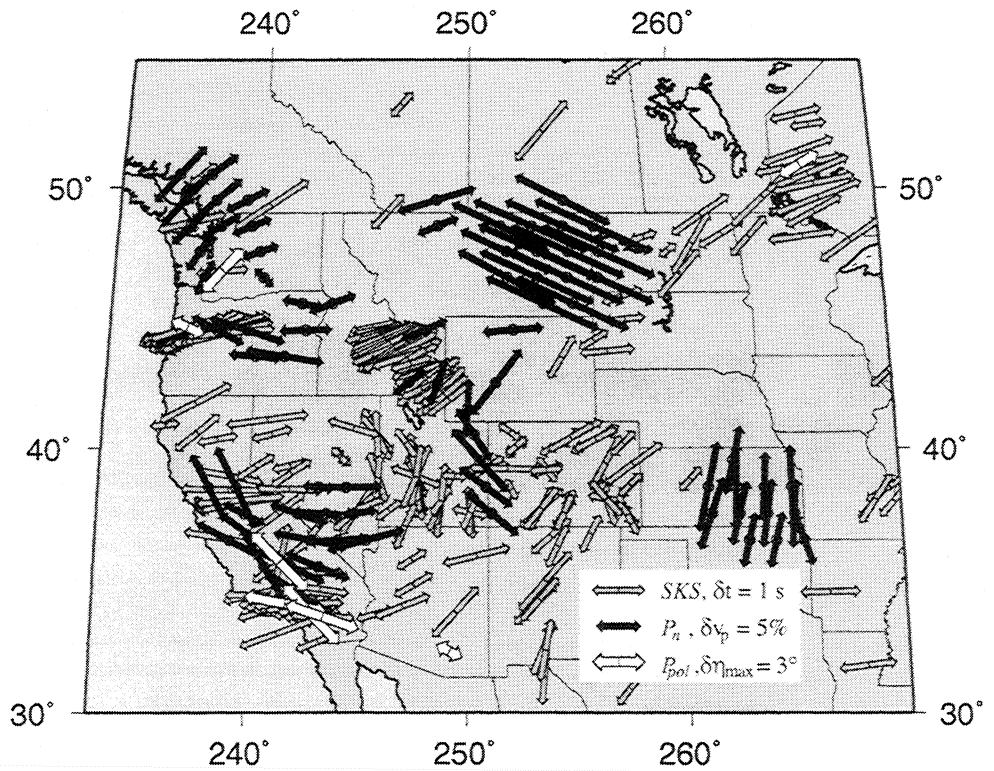

Figure 14. Comparison of anisotropic parameters from P_{pol} (white arrows), SKS (grey arrows) and P_n (black arrows): a closeup of western and central North America in Figure 12.

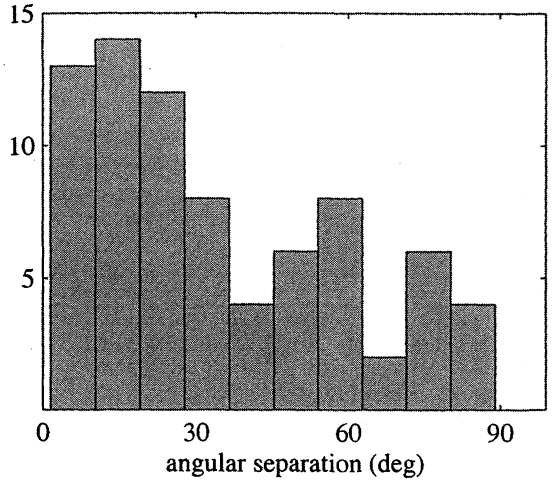

Figure 15. Histogram of the angular separation of individual measurements of $P_{\rm pol}$ versus P_n fast directions within 5° caps over the globe. All $P_{\rm pol}$ fast directions with an associated azimuthal error of >20° and significant amplitude are used.

was no correlation between the two methods, the angular separation should be uniformly distributed between 0° and 90°. Using the Kolmogorov-Smirnov statistic, we can say with 99.94% confidence that the observed differences are not uniformly distributed. The clustering toward small angles of separation suggests that the directions between the two data sets are regionally similar. The difference in sampling density over the globe does not bias this result, since the individual data sets have overall uniform distribution.

The *Smith and Ekström* [1999] P_n fast directions show a high internal consistency within 5° caps. In contrast, the SKS compilations have much more internal scatter. The distributions of the angular separation between SKS and P_n and between SKS and $P_{\rm pol}$ are also clearly nonuniform, but the influence of scatter in the SKS data set and a high density of SKS measurements in regions with systematic differences in fast directions (e.g., western United States and Europe) make the global correlation more complicated than in the $P_{\rm pol}$ versus P_n case. We will discuss the correlation region by region.

The depth sensitivity of the three methods can presumably be ranked as P_n as the shallowest, $P_{\rm pol}$ as intermediate, and SKS as deepest. Theoretically, SKS splitting can stem from any depth between the station and the core-mantle boundary. P_n, on the other hand, travels in the uppermost mantle, although the transition from the head wave to the diving P wave is less than clear cut. The depth sensitivity of our measurements was discussed in section 5.4. The depth range seen by our data set overlaps that of the other two methods except for deep-mantle SKS splitting.

There is a certain subjectivity associated with whether to interpret anisotropy directions in terms of lithospheric deformation or asthenospheric mantle flow. *Smith and Ekström* [1999] concentrate on lithospheric deformation, which appears reasonable for P_n. *Hearn* [1999] also invokes lithospheric compression and extension to explain P_n anisotropy directions as well as subduction and back arc-related flow. Although SKS results have been compared with World Stress Map horizontal directions of crustal compression [*Polet*, 1998], at least part of a splitting signal of the order of a second has to come from depths >100 km, unless the anisotropy is unusually strong. For SKS and $P_{\rm pol}$, and for P_n away from cratons, it seems appropriate to take mantle flow related to relative and absolute plate motion into consideration.

Areas with general agreement between all three methods can be speculated to have relatively shallow anisotropy, or at least little change in fast direction with depth. Within the error bounds, there appears to be agreement between $P_{\rm pol}$, P_n, and SKS fast directions in Japan, New Zealand, Alaska, the western United States and western and southern Europe. The active subduction and strike-slip zones, notably Japan, New Zealand, and California, are unlikely to have flow alignment that stays parallel going from the shallow to deep upper mantle. In these cases, it seems safe to assume that all three methods are picking up anisotropy in the uppermost mantle. Where P_n and P fast directions coincide and SKS shows a slight deviation, there may be some influence on SKS from anisotropy deeper than 250 km (Japan and Alaska). In areas where the $P_{\rm pol}$ fast direction is sandwiched between those from P_n and SKS, some of the deeper anisotropy influencing SKS may be sensed by $P_{\rm pol}$ (California and New Zealand).

Unfortunately, there are few areas on cratons that have P_n as well as SKS and $P_{\rm pol}$ measurements owing to seismicity constraints. For the majority of continental areas (e.g., Canada, Siberia, Scandinavia and Africa), SKS and $P_{\rm pol}$ appear to be in agreement, although there is a large scatter in the SKS compilation, presumably due to different methods, data sets, and frequency bands used. On the Canadian shield, the $P_{\rm pol}$ results agree with SKS and the direction of absolute plate motion [*Gripp and Gordon*, 1990]. The additional constraint provided by $P_{\rm pol}$ in these instances over having SKS measurements alone is that the anisotropy has to be situated at depths of no more than 250 km. Most cases where a large discrepancy is seen between $P_{\rm pol}$ and SKS involve a single SKS measurement.

Several regions show agreement between $P_{\rm pol}$ and P_n with a large discrepancy to SKS, notably Germany and the northernmost part of the western United States where SKS is nearly orthogonal to the other two solutions. In these cases, SKS is presumably sensing significant anisotropy at depths of >250 km. In the Pacific Northwest (Washington and British Columbia), P_n and $P_{\rm pol}$ undergo a rapid switch to a direction nearly orthogonal to that seen consistently along the the coastal western United States towards the south (Oregon and California), while SKS directions remain almost the same as farther south. However, a discrepancy between P and S fast directions may also suggest that our assump-

tion of horizontally symmetric hexagonal anisotropy is invalid in these areas.

Compilations of SKS fast directions show alignment parallel to strike slip faults [*Savage*, 1999]. Two exceptions cited by *Savage* [1999] are the San Andreas and North Anatolian faults. It is interesting that for both cases, our P_{pol} results show the expected fault-parallel fast directions, in contrast to SKS. Our data from station ANTO in Turkey yield an E-W fast axis, whereas *Vinnik et al.* [1992] inferred a NNE-SSW orientation from SKS, and *Hearn* [1999] and *Smith and Ekström* [1999] found little to no anisotropy in the vicinity from P_n measurements. Along the San Andreas fault both our P_{pol} and the P_n fit by *Smith and Ekström* [1999] yield fault-parallel orientations, while SKS studies have proposed E-W or two-layer splitting [*Savage*, 1999], and *Hearn* [1996] also obtained E-W orientation from a P_n inversion. Another strike-slip region with possible inconsistency between adjacent SKS observations is eastern Siberia [*Vinnik et al.*, 1992; *Savage*, 1999]. Again, our P_{pol} fast directions are fault-parallel and match one of two possibly contradicting SKS directions.

Anisotropic alignment from SKS and ScS splitting observed at oceanic island stations is generally perpendicular to the spreading direction [*Kendall*, 2000]. One exception was observed by *Wolfe and Silver* [1998] at Easter Island, where they found a N-S fast direction perpendicular to the plate motion. They attribute this to small-scale convection influenced by the presence of the Easter microplate. Our study supports the existence of the unusual orientation since the P_{pol} fast direction at RPN shows excellent agreement with the splitting result. We have no results at intraplate oceanic stations aside from Hawaii.

In Australia, where our results suggest alignment with the N-S absolute plate motion, published SKS and $SKKS$ results are highly contradictory, ranging from no splitting [*Özalaybey and Chen*, 1999] to significant splitting with trends of N-S [*Clitheroe and van der Hilst*, 1998] or E-W [*Vinnik et al.*, 1992]. In an analysis that is in some sense related to our own, *Girardin and Farra* [1998] inverted long-period P to S conversions at the single station CAN (Canberra) to obtain a two-layer model of anisotropy with an E-W fast direction in an upper and N-S in a lower layer at the top of the mantle. Models of azimuthal anisotropy derived from surface waves [*Debayle and Kennett*, 2000; *Montagner and Guillot*, 2000] show roughly E-W to NE-SW fast directions near 100 km depth and NE-SW to N-S near 200 km, which has been interpreted as absolute plate motion aligment in the asthenosphere and fossil deformation in the lithosphere. Our results apparently contradict this two-layer model, since our modeling suggests that P particle motion should be more sensitive to the upper layer. Clearly, more systematic forward modeling experiments are needed to clarify the effect of multiple anisotropic layers on P and S phases.

Surface waves can be inverted for depth-dependent anisotropy. In the past, most studies assumed transverse isotropy, which our measurements are insensitive to, but some global models of azimuthal anisotropy from surface waves have also been published [*Montagner and Guillot*, 2000]. When comparing such maps to Figure 12, it quickly becomes apparent that although there is agreement in some areas, the lateral resolution length of global surface wave studies of ~2000 km [*Montagner et al.*, 2000] is insufficient for comparison with body wave results. Regional surface waves can resolve lateral variations to ~350 km and as more azimuthal anisotropy maps from such studies become available, more accurate comparisons with body wave results will be possible.

6. Conclusions

We interpret transverse motion of long-period teleseismic P arrivals in terms of upper mantle anisotropy. The sensitivity of this new body wave anisotropy measurement is restricted to azimuthal anisotropy within one wavelength (maximum of 250 km) from the receiver. We obtain fast directions of the horizontal component of anisotropy by solving for $\sin(2\eta)$ azimuthal dependence of the particle motion deviation at each station. Modeling with a reflectivity code provides bounds for the strength and depth extent of anisotropy. Our fast axis directions can be compared to those from P_n travel times and SKS splitting. We find alignment parallel to the strike of orogenic belts, subduction zones, and transform faults, in agreement with P_n results. On cratons our results suggest alignment with absolute plate motion comparable to SKS splitting studies. These results are consistent with anisotropy influenced by lithospheric deformation at shallow depths and plate motion-induced flow in the deeper upper mantle.

Appendix A: Station Misorientation

As a by-product of the analysis of horizontal particle motion anomalies, we identified stations with horizontal sensor orientation problems. Several stations show a bias in horizontal particle motion that is constant over all arrival azimuths. These stations are suspected to have incorrectly oriented horizontal sensors. The misorientation is the constant term in the azimuthal least squares fit of (5). Other studies have made similar observations (*Laske* [1995] and *Larson* [2000] using surface waves and *Wang and McLaughlin* [1999] using body and surface waves), and we compare their misorientation values with ours in Figure A1. In most cases, the values agree within the error limits. A table of our misorientation values for these and more stations is available as an electronic supplement.

In addition to an overall misorientation of both horizontal sensors, there is also the possibility of a relative misalignment of the individual components, especially in instruments such as the STS-1 with physically separated sensors. However, the relative orientation should not be as prone to compass and surveying errors as the overall orientation appears to be.

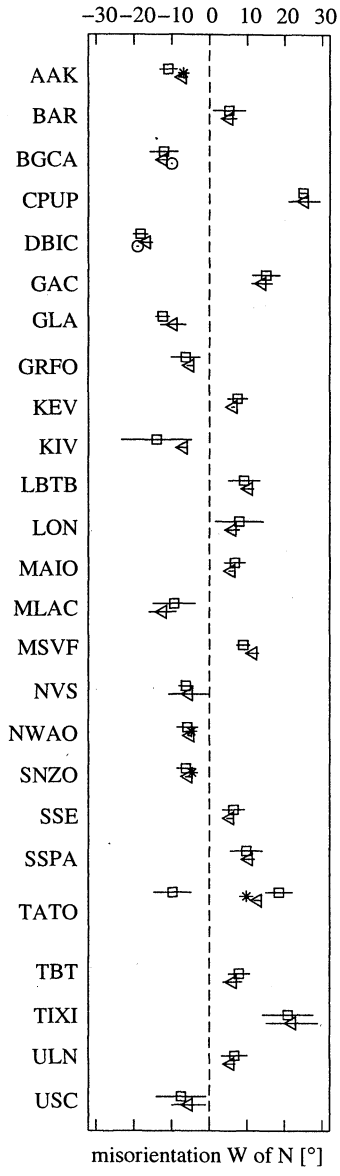

Figure A1. Estimates of horizontal sensor misorientation in degrees from four different studies. Squares are from this study, stars are from *Laske* [1995], triangles from *Larson* [2000], and circles (only BGCA and DBIC) are from *Wang and McLaughlin* [1999]. Different sign conventions were adjusted so that a positive value implies a counterclockwise rotation of the horizontal seismometer components. Our double symbol for TATO indicates an orientation shift in 1980.

Acknowledgments. The data used in this study were made available by the IRIS data management center. Paul Davis, Michael Kendall, Erik Larson, Jascha Polet, Martha Savage, Derek Schutt, and Gideon Smith graciously provided electronic versions of their *SKS*, P_n, and station misorientation results. We also thank Harold Bolton, Stuart Johnson, and Gabi Laske for providing some of the routines we used in the particle motion measurement and inversion codes, and Donna Blackman for helpful discussions. Comments by James Gaherty, Michael Kendall, and an anonymous reviewer greatly improved the quality of the manuscript. This work was supported by NSF grants EAR-9628494 and EAR-9902422.

References

Aki, K., and P. Richards, *Quantitative Seismology*, W.H. Freeman and Co., San Francisco, 1980.

Backus, G., Possible forms of seismic anisotropy of the uppermost mantle under oceans, *J. Geophys. Res.*, *70*, 3429–3439, 1965.

Baker, G., J. Minster, G. Zandt, and H. Gurrola, Constraints on crustal structure and complex Moho topography beneath Piñon Flat, California, from teleseismic receiver functions, *Bull. Seismol. Soc. Am.*, *86*, 1830–1844, 1996.

Barruol, G., A. Souriau, J. Vauchez, J. Diaz, J. Gallart, J. Tubia, and J. Cuevas, Lithospheric anisotropy beneath the Pyrenees from shear wave splitting, *J. Geophys. Res.*, *103*, 30,039–30,053, 1998.

Bokelmann, G., *P*-wave array polarization analysis and effective anisotropy of the brittle crust, *Geophys. J. Int.*, *120*, 145–162, 1995.

Booth, D., and S. Crampin, The anisotropic reflectivity technique: theory, *Geophys. J. R. Astron. Soc.*, *72*, 31–45, 1985.

Bostock, M., Mantle stratigraphy and evolution of the Slave province, *J. Geophys. Res.*, *103*, 21,183–21,200, 1998.

Chapman, C., and P. Shearer, Ray tracing in azimuthally anisotropic media – II. Quasi-shear wave coupling, *Geophys. J.*, *96*, 65–83, 1989.

Christensen, N., The magnitude, symmetry and origin of upper mantle anisotropy based on fabric analysis of ultramafic tectonites, *Geophys. J. R. Astron. Soc.*, *76*, 89–111, 1984.

Clitheroe, G., and R. van der Hilst, Complex anisotropy in the Australian lithosphere from shear-wave plitting in broadband *SKS* records, in *Structure and Evolution of the Australian Continent, Geodyn. Ser.* vol. 26, edited by J. Braun, pp. 73–78, AGU, Washington, D.C., 1998.

Crampin, S., R. Stephen, and R. McGonigle, The polarization of *P*-waves in anisotropic media, *Geophys. J. R. Astron. Soc.*, *68*, 477–485, 1982.

Debayle, E., and B. Kennett, Anisotropy in the australasian upper mantle from Love and Rayleigh waveform inversion, *Earth Planet. Sci. Lett.*, *184*, 339–351, 2000.

Dziewonski, A., Mapping the lower mantle: determination of lateral heterogeneity in *P* velocity up to degree and order 6, *J. Geophys. Res.*, *89*, 5929–5952, 1984.

Dziewonski, A., G. Ekström, and X.-F. Liu, Structure at the top and bottom of the mantle – two examples of use of broad-band data in seismic tomography, in *Monitoring a Comprehensive Test Ban Treaty, NATO ASI Series* vol. 303, edited by E. Husebye and A. Dainty, pp. 512–550, Kluwer Academic Publishers, Norwell, Mass., 1996.

Fabrititus, R., Shear-wave anisotropy across the Cascadia subduction zone from a linear seismography array, Master's thesis, Oregon State Univ., Corvallis, Oregon, 1995.

Fryer, L., and G. Frazer, Seismic waves in stratified anisotropic media, *Geophys. J. R. Astron. Soc.*, *78*, 691–710, 1984.

Girardin, N., and V. Farra, Azimuthal anisotropy in the upper mantle from observations of *P*-to-*S* converted phases: Applications to southeast Australia, *Geophys. J. Int.*, *133*, 615–629, 1998.

Grand, S., Mantle shear structure beneath the Americas and surrounding oceans, *J. Geophys. Res.*, *99*, 11,591–11,621, 1994.

Grand, S., R. van der Hilst, and S. Widiyantoro, Global seismic tomography: A snapshot of convection in the Earth, *GSA Today*, *7*, 1–7, 1997.

Gripp, A., and R. Gordon, Current plate velocities relative to the hotspots incorporating the NUVEL-1 global plate motion model, *Geophys. Res. Lett.*, *17*, 1109–1112, 1990.

Hearn, T., Anisotropic P_n tomography in the western United States, *J. Geophys. Res.*, *101*, 8403–8414, 1996.

Hearn, T., Uppermost mantle velocities and anisotropy beneath Europe, *J. Geophys. Res.*, *104*, 15,123–15,139, 1999.

Hu, G., W. Menke, and C. Powell, Polarization tomography for P wave velocity structure in southern California, *J. Geophys. Res.*, *99*, 15,245–15,256, 1994.

Humphreys, E., and R. Clayton, Tomographic image of the southern California mantle, *J. Geophys. Res.*, *95*, 19,725–19,746, 1990.

Jurkevics, A., Polarization analysis of three-component array data, *Bull. Seismol. Soc. Am.*, *78*, 1725–1743, 1988.

Kendall, J.-M., Seismic anisotropy in the boundary layers of the earth's mantle, in *Earth's Deep Interior: Mineral Physics and Tomography From the Atomic to the Global Scale, Geophysical Monograph Series* vol. 117, edited by S. Karato et al., pp. 149–175, AGU, Washington, D.C., 2000.

Kennett, B., *Seismic Wave Propagation in Stratified Media*, Cambridge Univ. Press, New York, 1983.

Krüger, F., and M. Weber, The effect of low-velocity sediments on the mislocation vectors of the GRF array, *Geophys. J. Int.*, *108*, 387–393, 1992.

Larson, E., Measuring refraction and modeling velocities of surface waves, Ph.D. thesis, Harvard Univ., Cambridge, Mass., 2000.

Laske, G., Global observation of off-great-circle propagation of long-period surface waves, *Geophys. J. Int.*, *123*, 245–259, 1995.

Laske, G., T. Masters, and W. Zürn, Frequency-dependent polarization measurements of long-period surface waves and their implications for global phase-velocity maps, in *10 Years of GEOSCOPE-Broadband Seismology*, edited by B. Romanowicz, pp. 111–137, Elsevier Sci., New York, 1994.

Levin, V., and J. Park, $P - SH$ conversions in layered media with hexagonally symmetric anisotropy: A cookbook, *Pure Appl. Geophys.*, *151*, 669–697, 1998.

Lilly, J., and J. Park, Multiwavelet spectral and polarization analyses of seismic records, *Geophys. J. Int.*, *122*, 1001–1021, 1995.

Lin, C.-H., and S. Roecker, P-wave backazimuth anomalies observed by a small-aperture seismic array at Piñon Flat, California: Implications for structure and source location, *Bull. Seismol. Soc. Am.*, *86*, 470–476, 1996.

Liu, X.-F., and J. Tromp, Uniformly valid body-wave ray theory, *Geophys. J. Int.*, *127*, 461–491, 1996.

Masters, G., S. Johnson, G. Laske, and H. Bolton, A shear-wave velocity model of the mantle, *Philos. Trans. R. Soc. London, Ser. A*, *354*, 1385–1411, 1996.

Masters, G., G. Laske, H. Bolton, and A. Dziewonski, The relative behavior of shear velocity, bulk sound speed, and compressional velocity in the mantle: implications for chemical and thermal structure, in *Earth's Deep Interior: Mineral Physics and Tomography From the Atomic to the Global Scale*, edited by S. K. et al., vol. 117 of *Geophys. Monogr. Ser.*, pp. 63–87, AGU, 2000.

Molnar, P., and P. Tapponnier, Cenozoic tectonics of Asia: Effects of a continental collision, *Science*, *189*, 419–426, 1975.

Montagner, J.-P., and L. Guillot, Seismic anisotropy in the Earth's mantle, in *Problems in Geophysics for the New Millenium*, edited by E. Boschi, G. Ekström, and A. Morelli, pp. 217–253, Editrice Compositori, Bologna, 2000.

Montagner, J.-P., D.-A. Pommera, and J. Lavé, How to relate body wave and surface wave anisotropy?, *J. Geophys. Res.*, *105*, 19,015–19,027, 2000.

Özalaybey, S., and W.-P. Chen, Frequency-dependent analysis of $SKS/SKKS$ waveforms observed in Australia; evidence for null birefringence, *Phys. Earth Planet. Inter.*, *114*, 197–210, 1999.

Park, J., C. Lindberg, and F. Vernon, Multitaper spectral analysis of high-frequency seismograms, *J. Geophys. Res.*, *92*, 12,675–12,684, 1987a.

Park, J., F. Vernon, and C. Lindberg, Frequency dependent polarization analysis of high-frequency seismograms, *J. Geophys. Res.*, *92*, 12,665–12,674, 1987b.

Polet, J., 1. Seismological observations of upper mantle anisotropy, 2. Source spectra of shallow subduction zone earthquakes and their tsunamigenic potential, Ph.D. thesis, Calif. Inst. of Technol., Pasadena, 1998.

Pondrelli, S., and R. Azzara, Upper mantle anisotropy in Victoria Land (Antarctica), *Pure Appl. Geophys.*, *151*, 433–442, 1998.

Powell, C., and B. Mitchell, Relative array analysis of the southern California lithosphere, *J. Geophys. Res.*, *99*, 15,257–15,275, 1994.

Richards-Dinger, K., and P. Shearer, Estimating crustal thickness in couthern California by stacking PmP arrivals, *J. Geophys. Res.*, *102*, 15,211–15,224, 1997.

Rümpker, G., and P. Silver, Apparent shear-wave splitting parameters in the presence of vertically varying anisotropy, *Geophys. J. Int.*, *135*, 790–800, 1998.

Russo, R., and P. Silver, Trench-parallel flow beneath the Nazca plate from seismic anisotropy, *Science*, *263*, 1105–1111, 1994.

Saltzer, R., J. Gaherty, and T. Jordan, How are vertical shear wave splitting measurements affected by variations in the orientation of azimuthal anisotropy with depth?, *Geophys. J. Int.*, *141*, 374–390, 2000.

Savage, M., Lower crustal anisotropy or dipping boundaries: Effects on receiver functions and a case study in New Zealand, *J. Geophys. Res.*, *103*, 15,069–15,087, 1998.

Savage, M., Seismic anisotropy and mantle deformation: What have we learned from shear wave splitting?, *Rev. Geophys.*, *37*, 65–106, 1999.

Savage, M., and A. Sheehan, Seismic anisotropy and mantle flow from the Great Basin to the Great Plains, western United States, *J. Geophys. Res.*, *105*, 13,715–13,734, 2000.

Savage, M., A. Sheehan, and A. Lerner-Lam, Shear wave splitting across the Rocky Mountain front, *Geophys. Res. Lett.*, *23*, 2267–2270, 1996.

Shearer, P., and C. Chapman, Ray tracing in azimuthally anisotropic media - I. results for models of aligned cracks in the upper crust, *Geophys. J.*, *96*, 51–64, 1989.

Silver, P., Seismic anisotropy beneath the continents: Probing the depths of geology, *Annu. Rev. Earth Planet. Sci.*, *24*, 385–432, 1996.

Smith, G., and G. Ekström, A global study of P_n anisotropy beneath continents, *J. Geophys. Res.*, *104*, 963–980, 1999.

Vidale, J., Complex polarization analysis of particle motion, *Bull. Seismol. Soc. Am.*, *76*, 1393–1405, 1986.

Vinnik, L., and J.-P. Montagner, Shear wave splitting in the mantle Ps phases, *Geophys. Res. Lett.*, *23*, 2449–2452, 1996.

Vinnik, L., L. Makeyeva, A. Milev, and A. Usenko, Global petterns of azimuthal anisotropy and deformations in the continental mantle, *Geophys. J. Int.*, *111*, 433–447, 1992.

Wagner, G., Regional wave propagation in southern California and Nevada: Observations from a three-component seismic array, *J. Geophys. Res.*, *102*, 8285–8311, 1997.

Wang, J., and K. McLaughlin, Global slowness-azimuth station calibrations for the IMS network, *Memo CCB-PRO-99/02*, Center for Monitoring Research, Arlington, Va., 1999.

Wolfe, C., and P. Silver, Seismic anisotropy of oceanic upper mantle: Shear wave splitting methodologies and observations, *J. Geophys. Res.*, *103*, 749–771, 1998.

Wolfe, C., and S. Solomon, Shear-wave splitting and implications for mantle flow beneath the MELT region of the East Pacific Rise, *Science*, *280*, 1230–1232, 1998.

Wolfe, C., F. Vernon, and A. Abdullah, Shear-wave splitting across western Saudi Arabia: The pattern of upper mantle anisotropy at a Proterozoic shield, *Geophys. Res. Lett.*, *26*, 779–782, 1999.

Zhu, L., and H. Kanamori, Moho depth variation in southern California from teleseismic receiver functions, *J. Geophys. Res.*, *105*, 2969–2980, 2000.

G. Masters, V. Schulte-Pelkum, and P. M. Shearer, Institute of Geophysics and Planetary Physics, Scripps Institution of Oceanography, University of California, San Diego, La Jolla, CA 92093-0225, USA. (vschulte@ucsd.edu)

(Received July 17, 2000; accepted April 3, 2001.)